

See discussions, stats, and author profiles for this publication at: <https://www.researchgate.net/publication/260939843>

# At the frontiers of high-resolution hard-X-ray microscopy: an international programm

Article in *Journal of Physics D Applied Physics* · December 2013

DOI: 10.1088/0022-3727/46/49/494005

---

CITATIONS

4

---

READS

101

7 authors, including:



**Yong S Chu**

Brookhaven National Laboratory

268 PUBLICATIONS 4,178 CITATIONS

[SEE PROFILE](#)



**G. Margaritondo**

École Polytechnique Fédérale de Lausanne

1,059 PUBLICATIONS 17,249 CITATIONS

[SEE PROFILE](#)

Some of the authors of this publication are also working on these related projects:



Venice Time Machine [View project](#)



Brain cancer [View project](#)

## At the frontiers of high-resolution hard-x-ray microscopy: an international programme

This content has been downloaded from IOPscience. Please scroll down to see the full text.

2013 J. Phys. D: Appl. Phys. 46 494005

(<http://iopscience.iop.org/0022-3727/46/49/494005>)

View [the table of contents for this issue](#), or go to the [journal homepage](#) for more

Download details:

IP Address: 128.178.174.235

This content was downloaded on 02/12/2014 at 16:42

Please note that [terms and conditions apply](#).

# At the frontiers of high-resolution hard-x-ray microscopy: an international programme

S R Wu<sup>1,2</sup>, C H Lin<sup>1</sup>, Y S Chen<sup>1</sup>, Y Y Chen<sup>1</sup>, Y Hwu<sup>1,2,3,6</sup>, Y S Chu<sup>4</sup>  
and G Margaritondo<sup>5</sup>

<sup>1</sup> Institute of Physics, Academia Sinica, Taipei 115, Taiwan

<sup>2</sup> Department of Engineering and System Science, National Tsing Hua University, Hsinchu 300, Taiwan

<sup>3</sup> Advanced Optoelectronic Technology Center, National Cheng Kung University, Tainan 701, Taiwan

<sup>4</sup> NSLS-II, Brookhaven National Laboratory, Upton, NY 11973-5000, USA

<sup>5</sup> Faculté des Sciences de Base, École Polytechnique Fédérale de Lausanne (EPFL), CH-1015 Lausanne, Switzerland

E-mail: [phhwu@sinica.edu.tw](mailto:phhwu@sinica.edu.tw)

Received 18 April 2013, in final form 26 August 2013

Published 22 November 2013

Online at [stacks.iop.org/JPhysD/46/494005](http://stacks.iop.org/JPhysD/46/494005)

## Abstract

We review the recent progress achieved by our international collaboration on novel imaging techniques based on high-brightness and highly coherent synchrotron sources. After outlining the background, we will discuss the technical progress of recent years. Then, we will exemplify the applications with a number of cases in materials science and life sciences, in particular neurobiology. New results on metal electrodeposition will be used to practically illustrate the impact of the techniques in this important technological area and in general its potential for materials research. Finally, we will briefly comment on the foreseeable technical improvements and on their positive consequences.

(Some figures may appear in colour only in the online journal)

## 1. Background

Microscopy using x-rays, in particular hard x-rays, had quite a limited scope during the first century after Roentgen's discovery [1]. This was primarily due to technical problems of two kinds. First, the brightness produced by x-ray sources was quite limited: since (Liouville theorem) the brightness is conserved in a lossless optical system, this had a negative impact on all applications and in particular on microscopy.

The second technical problem affected the optical components. Refraction, the standard mechanism to fabricate optical devices for visible light, is very inefficient for x-rays since the real part of the complex refractive index is close to unity. Reflection is also inefficient except at low grazing angles. And the short wavelengths impose very stringent technical requirements on the micromorphology of the optical devices.

This disappointing situation radically changed in recent years, with a real and potential impact on a variety of research

domains. Indeed x-rays, thanks to their high penetration in condensed matter, the extreme values of their microscopy diffraction limit and their spectroscopic properties, are an ideal instrument to explore systems on the nanoscale. The recent developments start to unlock their potential [2–11].

The two key elements in these developments match the aforementioned difficulties. First, the progress in synchrotron radiation sources [12] now provides x-rays of very high brightness. This is primarily the result of progress in the geometry of the emission, and therefore implies a simultaneous improvement in lateral coherence. Modern synchrotron sources are indeed reaching the diffraction limit for lateral coherence in a non-negligible part of their emitted spectrum.

Second, the source progress was accompanied and complemented by significant improvements in the technology of x-ray optical devices [13]. This actually affected several classes of devices, although in this paper we concentrate on x-ray Fresnel zone plates (FZPs). As a consequence, key parameters such as the lateral resolution have rapidly improved over the past ten years, reaching now levels close to 10 nm with no foreseeable saturation of the progress [14].

<sup>6</sup> Author to whom any correspondence should be addressed.

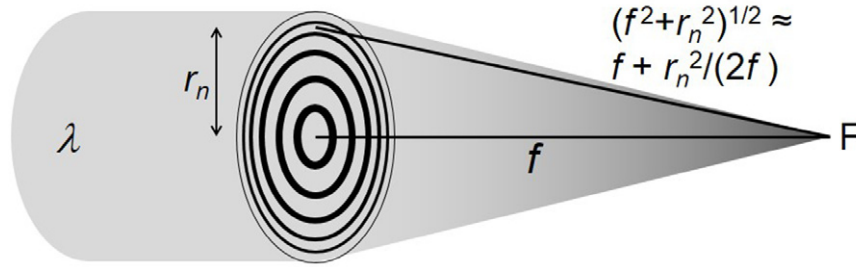


Figure 1. Simplified scheme of an FZP.

Our objective here is not to present a comprehensive history of these developments but to give the reader a flavour of our own experience in this rapidly evolving field; we will present the most recent milestones in our programme and exemplify their applications to research. This last task will be accomplished, in particular, by discussing in detail the microradiology analysis of electrochemical processes, which, historically, produced surprising results like metal films building on gas bubbles [15].

Finally, we shall discuss the probable developments in the near future. This is a relevant part of our review because of the rapid developments in a new class of x-ray sources, the free electron lasers (X-FELs) [16]. Quite recently, scientists at Elettra in Trieste demonstrated [17] the first application of seeding in this domain, opening up an entirely new domain of applications that could further revolutionize hard-x-ray microscopy and deserve special attention.

## 2. Development of a hard-x-ray microscopy project

Our team has been involved in the development of x-ray microradiology with synchrotron radiation since the late 1990s. We were particularly interested in the fabrication of advanced FZPs to focus low-wavelength radiation. Recently, the technical evolution for hard x-rays has been significantly accelerated [18–45].

FZPs are an effective response to the challenge of fabricating optical devices for low wavelengths. X-ray focusing cannot use the standard mechanisms for visible optics, reflection and refraction. Calling  $1 - \delta - i\beta$  the index of refraction, x-rays are effectively reflected only at grazing angles below  $\approx (2\delta)^{1/2}$ , a very small value of a few hundredths of a radian for hard x-rays. Thus, reflection-based x-ray optics must work at extremely small grazing angles, facing big technical challenges. Refraction by materials is also very ineffective because of the small value of  $\delta$ .

This makes FZPs, which are based on interference, particularly attractive. A circular FZP (figure 1) includes alternating absorbing and transmitting concentric zones. Constructing interference produces focusing according to the condition

$$(f^2 + r_n^2)^{1/2} - f = n\lambda, \quad (1)$$

where  $r_n$  is the radius of the  $n$ th zone,  $\lambda$  is the wavelength and  $f$  is the focal distance. For x-rays  $\lambda$  is small, thus  $r_n \ll f$ , thus  $(f^2 + r_n^2)^{1/2} \approx f[1 + r_n^2/(2f^2)]$ , and

$$r_n \approx (2n\lambda f)^{1/2}. \quad (2)$$

The conditions for the spatial resolution  $\Delta x$  are derived [9] from this equation using the Rayleigh criterion:

$$\Delta x \approx 1.22(f/D)\lambda,$$

where  $D$  is the FZP diameter. Calling  $r_m$  the outermost zone radius,  $D = 2r_m$  and

$$\Delta x \approx 1.22 f\lambda / (2r_m). \quad (3)$$

Thus, the resolution is related to the outermost zone width. Note that the width  $\Delta r_m$  of the transparent outermost zone (see equation (2)) is

$$\begin{aligned} & [(2m\lambda f)^{1/2} - [2(m-1)\lambda f]^{1/2}]/2 \\ &= (2m\lambda f)^{1/2} \{1 - [(m-1)/m]^{1/2}\} / 2 \\ &\approx (2m\lambda f)^{1/2} [1/(2m)] / 2 = \lambda f / [2(2m\lambda f)^{1/2}] \\ &= \lambda f / 2r_m, \text{ and} \end{aligned}$$

$$\Delta x \approx 1.22 \Delta r_m. \quad (4)$$

In other words, the lateral resolution of an FZP is as good as our capability to produce very narrow outermost zones. This poses formidable technical challenges, since the opaque zones must be thick enough to absorb x-rays, whose absorption coefficient is very small. Thus, x-ray FZPs require outermost zones with a large ‘aspect ratio’, the ratio between thickness and width. Achieving a large aspect ratio creates huge fabrication problems and the risk of mechanical instability.

Furthermore, since  $D = 2r_m = \lambda f / (2\Delta r_m)$ , a narrow outermost zone corresponds to a small diameter: x-ray FZPs are very small objects. Assuming typical values  $\lambda = 1 \text{ \AA}$ ,  $f = 3 \text{ cm}$ ,  $\Delta r_m = 20 \text{ nm}$ , we get indeed  $D \approx 75 \text{ }\mu\text{m}$ .

FZPs can also exploit [13, 30, 46] higher order focusing at  $f/3$  and at the other odd fractions of the first-order focus. However, the efficiency progressively decreases.

Efficiency, i.e. the fraction of radiation power that is focused, is indeed a key problem for FZPs. One limiting factor is the absorption by the absorbing zones. Another is the focusing not at the first-order point but at higher orders or at infinity. One can show [13] that maximum efficiency occurs when neighbouring absorbing and transmitting zones have equal widths and that the first-order efficiency is

$$E = 1/\pi^2 \approx 10\%. \quad (5)$$

For  $q$ th order focusing, one obtains

$$E = 1/(q\pi)^2. \quad (6)$$

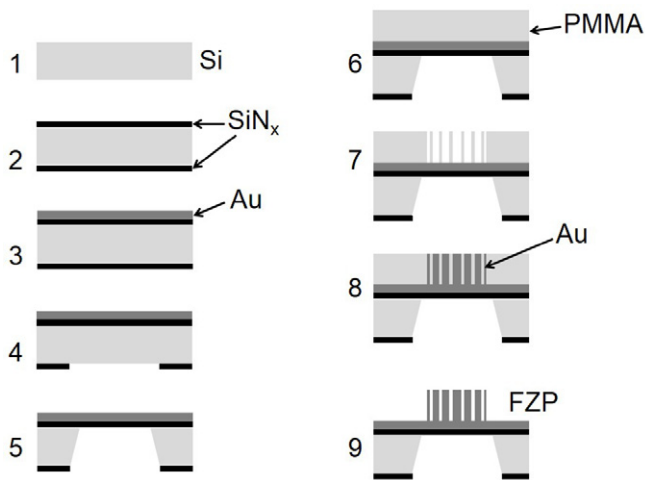


**Figure 2.** Scheme of our process for fabrication of FZPs, using e-beam lithography and electrodeposition: (1) and (2) coating of a Si wafer with silicon nitride, (3) Au deposition, (4) and (5) opening of a window, (6) coating with PMMA, (7) patterning by e-beam lithography, (8) electrodeposition of Au in the pattern trenches and (9) PMMA removal.

The efficiency can be improved, however, by using zones that are not strongly absorbing but shift the phase [13, 47], and eliminate the power lost to focusing at infinity. The theoretical first-order value climbs in that case from 10% to >40%.

These theoretical values for pure absorption or pure phase shift, however, are not quite realistic since the ‘opaque’ zones of a real FZP produce both phase shifting and absorption. As a consequence, the efficiency optimization in realistic cases requires a compromise between the material composition, the FZP geometry—in particular the zone widths—and the FZP thickness. With such a choice, the theoretical effectiveness can indeed exceed 40%.

### 2.1. Nanofabrication challenges

The challenges posed by the production of efficient x-ray FZPs were tackled with a variety of approaches, including dry etching with a hard mask and atomic layer deposition (ALD) [27, 28, 48]. Our own programme is based on electron-beam (e-beam) lithography and electrodeposition; a process is schematically shown in figure 2.

The first step of this approach [13] consists in depositing on both sides of a silicon wafer a silicon nitride film by low-pressure chemical vapour deposition (LPCVD). On one of the two sides, one then thermally deposits a medium-thickness gold film.

From the silicon wafer thus processed, one obtains squares of the order of a few mm. For each square, a window is created on the side with no Au film by removing the nitride with reactive ion etching (RIE). Chemical etching then eliminates the silicon under the window. The result in the window area is a nitride film covered by gold.

The next step requires creating a photoresist film by spin-coating poly(methyl methacrylate) or PMMA whose thickness can reach the  $\mu\text{m}$  level. This is the material on which the FZP pattern can be ‘written’, the writing being

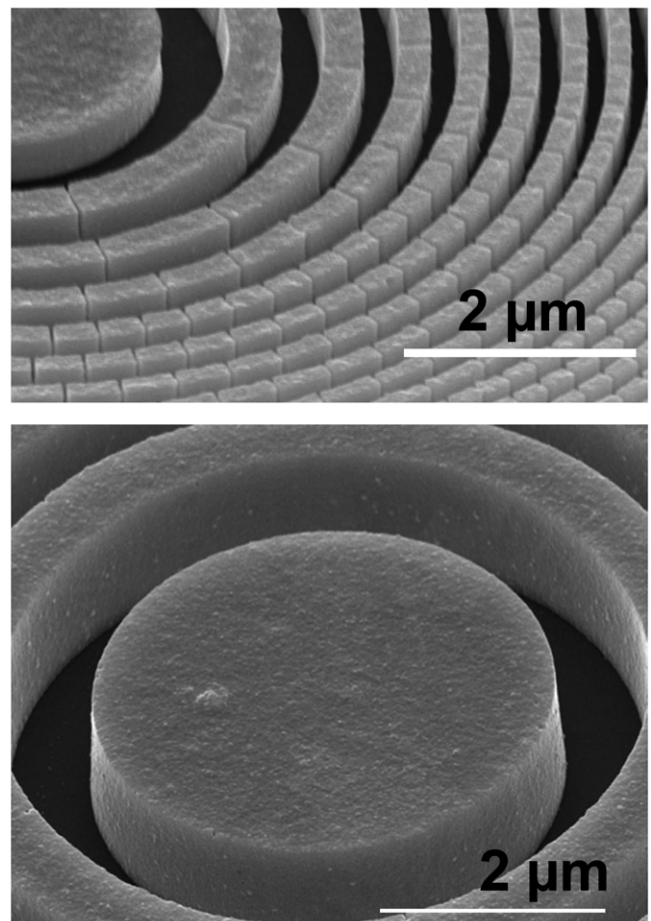


**Figure 3.** Two scanning electron micrographs of our FZPs, emphasizing the thickness of the Au pattern as required to obtain strong x-ray absorption.

performed by advanced e-beam lithography. After writing, a ‘negative’ pattern is produced by developing the PMMA and then eliminating residues with ultrasound cleaning.

The final step is the electrodeposition of gold inside the ‘trenches’ that form the negative FZP pattern in the PMMA. After eliminating the PMMA by chemical processing, what is left is the positive FZP pattern in gold over the Au-coated nitride membrane.

Refinements of this procedure have produced over the recent years a progressive improvement in the FZP quality and performances. This was the result of a painstaking optimization of the many different fabrication steps and of the search of the best compromises between the different parameters. The progress is not over and further improvements are possible. However, the achieved performances already open the way to exciting new research opportunities in a variety of domains.

### 2.2. The progressive enhancement of resolution

Figures 3–5 illustrate some of the results of this optimization. Specifically, we see examples of hard-x-ray FZPs with narrow outermost zones, high aspect ratio and very good mechanical stability. Figures 6–8 show examples of the images produced

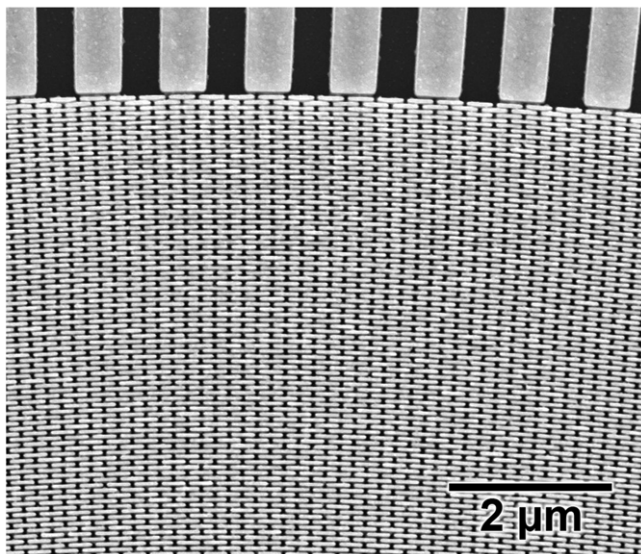


**Figure 4.** Scanning electron micrograph of the margin of one of our FZPs; the outermost zone width is 30 nm.

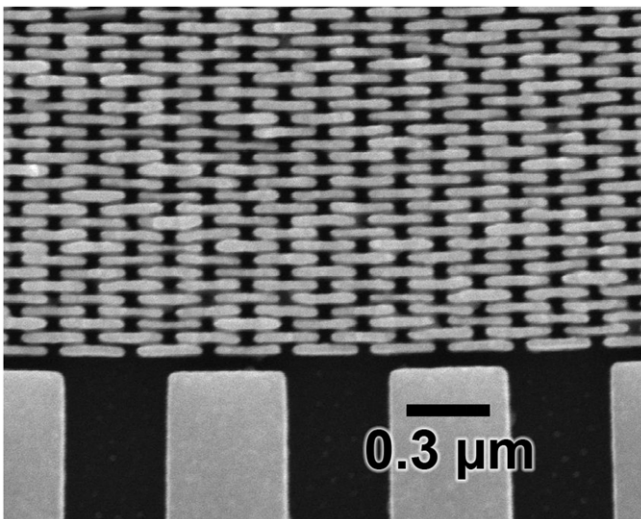


**Figure 5.** Zoomed scanning electron micrograph similar to that of figure 4, showing an FZP with 20 nm outermost zone width.

by these devices. In particular, figure 6 shows micrographs of a mask used for the lithography step in the fabrication of our FZPs, with 40 nm outermost zone width. Figure 7 refers to a periodic Si–SiMo multilayer with 15 nm periodicity. Figure 8 shows an anodized  $\text{Al}_2\text{O}_3$  slab with pores produced by chemical etching, filled by BeTe; the pore diameter is approximately 30 nm.

The overall resolution progress over time for our programme is illustrated by figure 9 [14]. We see from the image quality and from the quantitative estimates of the resolution the fast track towards the present levels, 15 nm, and towards the envisioned targets beyond 10 nm.

These results raise the important issue of how the resolution is measured [13]. This is a delicate point since there is no convergence in the literature towards a single method and a single criterion. In some cases, comparisons can be misleading or unfair.

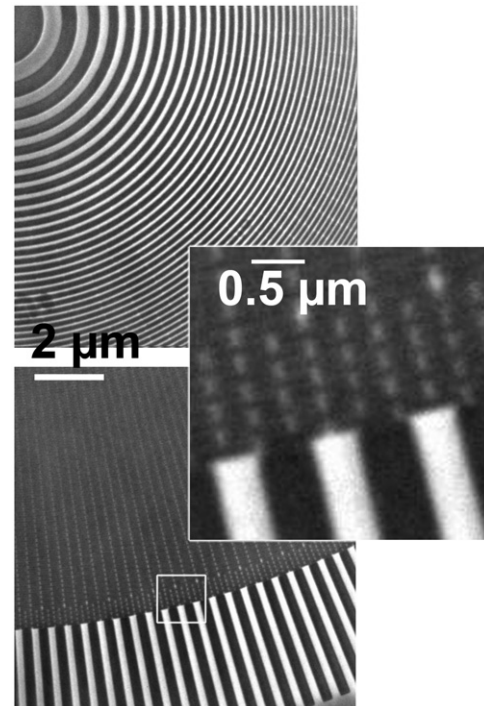


**Figure 6.** Test of the performances of our FZPs: micrograph of a mask used for lithography in FZP fabrication, with 40 nm outermost zone width.

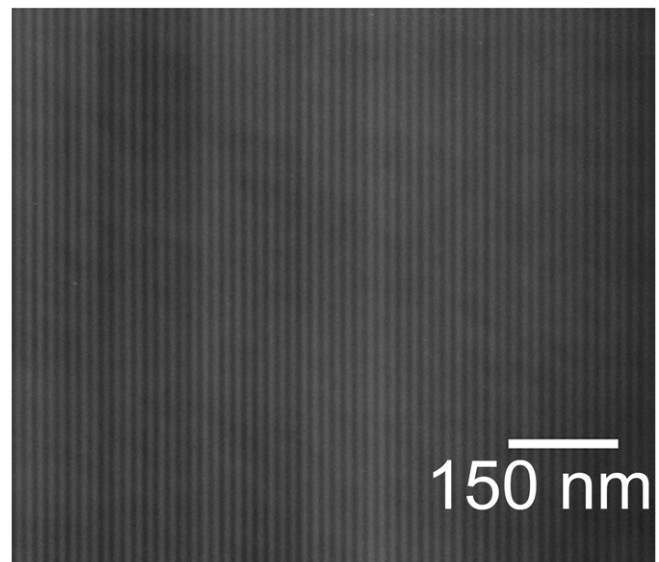


**Figure 7.** Microradiography of a periodic Si–SiMo multilayer with 15 nm periodicity.

Among the adopted standards, a popular one is the Rayleigh criterion, theoretically related (equation (4)) to the outermost zone width [13]. This theoretical value, however, can be an overestimate in practical cases. In fact, it does not take into account the important role of noise or, better, of the noise-to-signal ratio.

A second approach [13] is empirical and based on the smallest features that can be detected by somebody analysing the image. In addition to its subjective character, this method has other limitations that tend to overestimate the actual resolution.

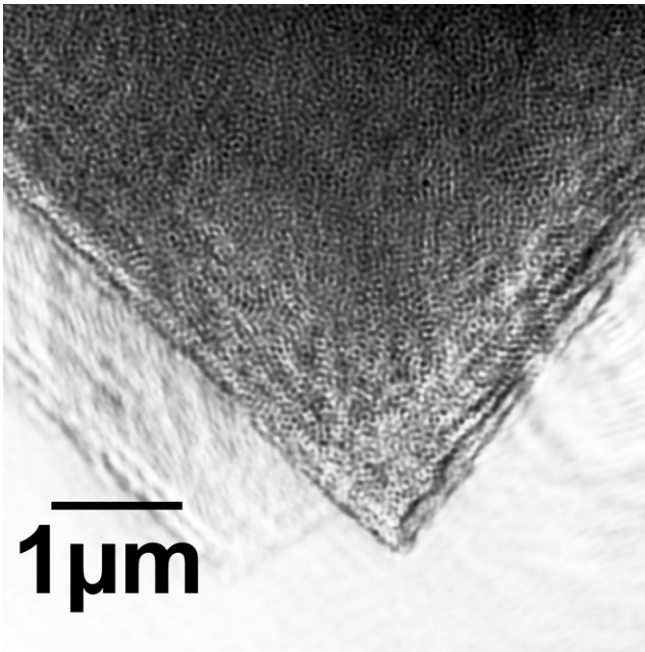


**Figure 8.** Microradiography of an anodized  $\text{Al}_2\text{O}_3$  slab with pores produced by chemical etching and filled by BeTe. The typical pore diameter is  $\approx 30$  nm.

Thirdly, one can use line scans, selecting features in the images with an edge presumably narrower than the resolution and measuring the intensity in the direction perpendicular to it [13]. If one neglects the effects of the edge width and assumes only instrumental broadening, the distance between the points with 20% and 80% intensity equals 1.68 times the Gaussian-broadening parameter  $\sigma$ . In turn, the Raleigh resolution is  $\approx 2.77$  times this parameter. The limitation of this approach is primarily linked to the hypothesis of negligible effects of the edge widths.

Other definitions of the resolution [13] realistically take into account the noise. Specifically, the power spectrum analysis (PSA) method Fourier-transforms the intensity of an image, takes the square and then the azimuthal integral. Before the Fourier transform, the image is normally filtered with a window function to mitigate edge effects. The high frequency cutoff of the Fourier spectrum presumably corresponds to the smallest features in the image. If the intrinsic feature size is smaller than the resolution, then the frequency cutoff is related to the resolution.

Finally, the modulation transfer function (MTF) method is best applied to test patterns with periodic lines of different spatial frequencies. Calling  $I_{\max}$  and  $I_{\min}$  the maximum and minimum intensities of the line series in the image, the MTF is defined as  $(I_{\max} - I_{\min})/I_{\max}$ . By plotting the MTF as a function of the line spatial frequency one can derive the resolution. Specifically, the so-called ‘Raleigh contrast resolution’ corresponds to  $I_{\min}/I_{\max} \approx 0.735$ . Presumably, this approach and those related to it automatically take into account the noise effects.

Whatever criterion is adopted to define resolution, the progress of recent years is evident. The forthcoming benchmark of 10 nm can be realistically defined, for example, in terms of Raleigh resolution and contrast.

### 3. Recent advances

As already mentioned, along the path towards this benchmark the best resolution so far of hard-x-ray FZPs is  $\approx 15$  nm [14]. This level is derived with the Rayleigh contrast criterion described above.

In addition to this impressive resolution level, hard-x-ray FZPs offer several other positive features. A very important one is of course the penetration of x-rays and the corresponding possibility to study three-dimensional properties without very thin sectioning of the specimens.

Furthermore, in addition to projection imaging we demonstrated the feasibility of tomographic reconstruction without sacrificing the spatial resolution and with limited artefacts [29, 49]. This considerably extends the possibility of analysing, in detail, three-dimensional properties on the nanoscopic scale [50].

High-resolution imaging with advanced FZPs was also implemented using the classic technique of Zernike phase contrast [22, 51, 52]. The results show a marked improvement in the image quality—in particular the contrast—without deterioration in the resolution level.

As already mentioned, FZPs offer the opportunity to work not only with first-order focusing but also with higher (odd) orders [10, 13, 46]. The advantage is of course a better resolution, but at the cost of a reduced throughput. Higher order imaging was indeed demonstrated in several cases [10, 13, 46, 53], enhancing the resolution performances of this type of microscopy.

Another important development is imaging in a dark-field configuration [54, 55]. This means detecting only scattered waves and eliminating the unscattered transmitted waves. The advantages are comparable to those of dark-field microscopy in the visible range. This approach has been recently demonstrated for hard-x-ray FZPs [54].

Another rapidly evolving technique for hard-x-ray microscopy is coherent diffraction imaging (CDI) [56]. A comprehensive discussion of this technique and its applications is beyond the scope of this work. We would like to mention, however, that hard-x-ray zone plates were used in these studies to create curved-field illumination [57]. The results of CDI in analysing three-dimensional structures, particularly of biological specimens [58, 59], are of quality comparable to those of transmission x-ray microscopy.

In addition to the improvements in the FZPs and in their use, important advances were obtained in collateral fields. One of the most important is the development of suitable contrast agents for x-ray microscopy, a need not satisfied by standard methods for visible and electron microscopy [14].

The most important applications of the advances in x-ray FZP performances are in biomedical research. We show in figures 10–12 some recent examples. Specifically, figure 10 corresponds to a thick tissue section of a mouse aorta [49]. Clearly visible in the images are the boundaries of the vessel (marked by dashed lines) and red blood cells inside. The nuclei of endothelial cells are also easily seen. Note the three-dimensional character of this specimen: the capability to analyse structures in three dimensions makes hard-x-ray microscopy particularly powerful for tissue analysis.

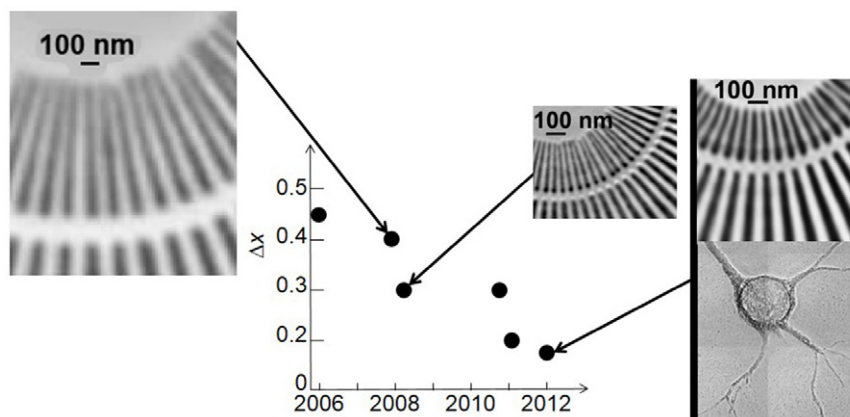


**Figure 9.** Progress in hard-x-ray FZP performances in recent years, illustrated by the spatial resolution  $\Delta x$  and by selected images; figure from [10].

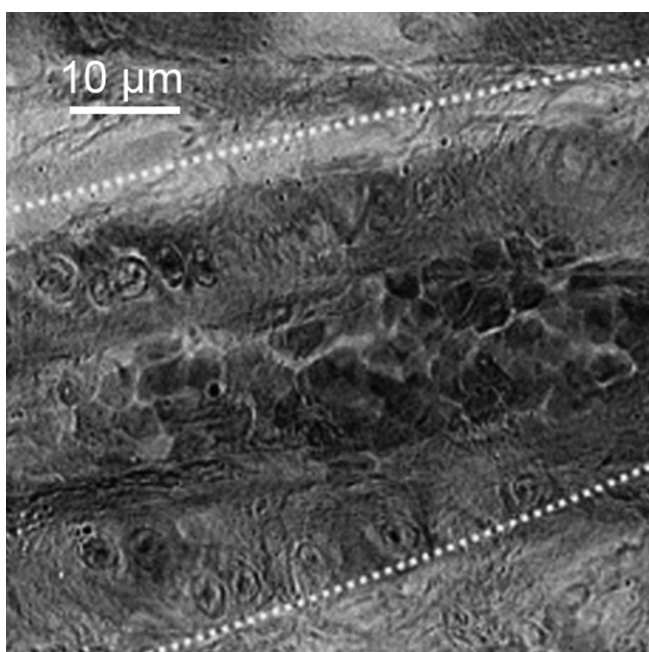


**Figure 10.** Micrograph of a thick tissue section of a mouse aorta [49]. Note the vessel boundaries (marked by dashed lines) and the red blood cells inside. Also visible are the nuclei of endothelial cells.

Figure 11 shows three images of a neuron specimen from a mouse brain [14]. The progressive zooming reveals fine details of the cellular structure and of the interconnections. These images demonstrate that hard-x-ray FZP microscopy is now capable of working at the subcellular level for animal specimens. They are also a demonstration of effective staining, in this case with the Golgi-Cox procedure. Here again we see the advantages of hard-x-ray penetration: the specimen was 50  $\mu\text{m}$  thick.

Figure 12 shows the micrograph of a HeLa cancer cell. The dark spots reveal bare Au nanoparticles and nanoparticle agglomerates that selectively accumulated at the periphery of the nuclei. In this case, the cells were cultured on a Petri dish. This result demonstrates the recent advances in staining: the nanoparticles clearly reveal the nucleus.

Figures 13–15 illustrate representative results of tomographic reconstruction. In figure 13, we see some examples

from a set of 280 raw projection images of neuron cells from mouse brain, taken at equal angular distances in the range from  $-70^\circ$  to  $70^\circ$ . From this image set, reconstruction can yield any desired view, such as the three examples of figure 14. Figure 15 shows a set of reconstructed images (from different angular points of view) of a HeLa cell similar to that of figure 12, including bare Au nanoparticles.

The above performances for cell imaging should be compared with those of other techniques using x-rays. For example, the above-mentioned CDI technique offers certain advantages for whole cell imaging [60], which are potentially important for X-FEL sources.

Soft-x-ray transmission microscopy achieved lateral resolution levels similar to hard-x-ray microscopy and was extensively applied to biological specimens [61, 62]. Taking advantage of the water-window where soft x-rays produce high contrast on carbon and water [63, 64], substantial structural information at the subcellular level could be obtained without heavy metal staining, with the radiation damage minimized by cryogenic conditions [65]. The lower penetration and stronger scattering with respect to hard x-rays, however, limit the applications of soft-x-ray microscopy to single cell level [66]. Specific optical microscopies were proposed to complement soft-x-ray microscopy and obtain simultaneous imaging of the same subcellular area [67].

We note that the development of new x-ray sources based on compact accelerators [68] or other approaches is potentially important to the development of x-ray microscopy. Currently, their brightness in the x-ray range is still far from synchrotron sources. However, they are rapidly improving and benefit from new technology discoveries [69, 70]. Thus, their small size and easy access could play in favour of these laboratory-based sources for specific critical applications, notably related to biological specimens. These developments are potentially an advantage for soft-x-ray microscopy because the new sources are much more difficult to develop for shorter wavelengths.

#### 4. An example of applications: electrochemistry processes

Electrodeposition is a widely used industrial process that still has many unclear issues [15]. In most cases, the morphology

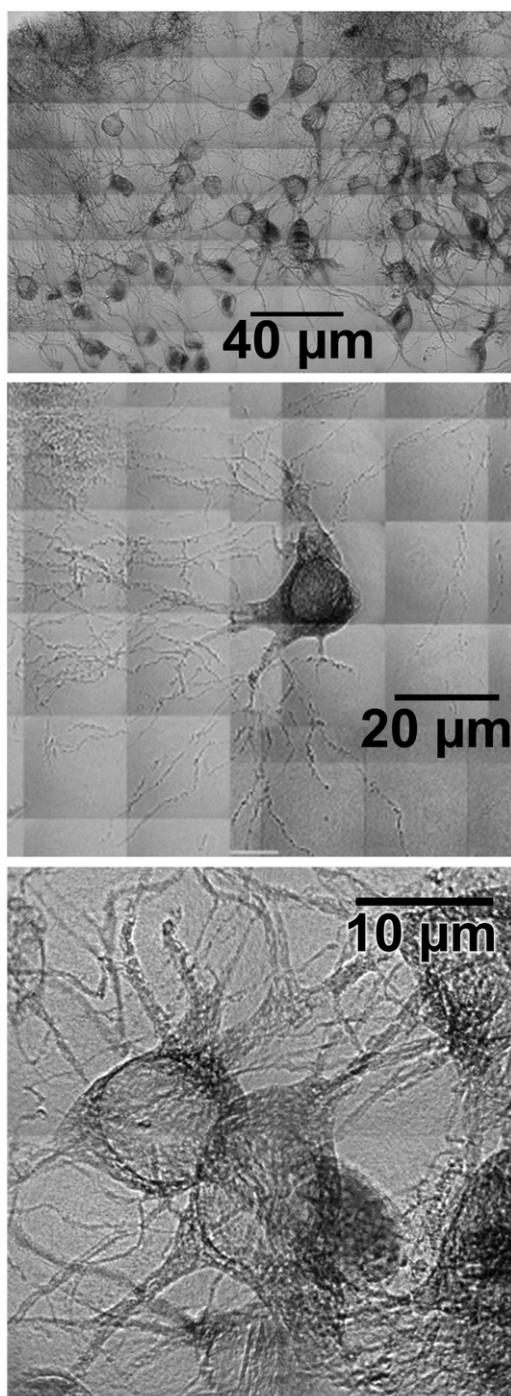


**Figure 11.** Micrographs of a neuron specimen from a mouse brain [14].

on the scale of tens of nanometres plays an important and so far largely unexplored role. Therefore, x-ray microscopy is an ideal instrument to clarify the still unknown features.

Several examples of x-ray microscopy studies of this process appeared in the recent literature [15, 18, 71–73]. One of the most relevant was the clarification in 2002 of the role of bubbles in the electrodeposition of Zn over Zn [15]. Quite surprisingly, the direct observation of the process by microradiology revealed Zn growing directly on fast-disappearing bubbles, thus leading to the creation of cavity

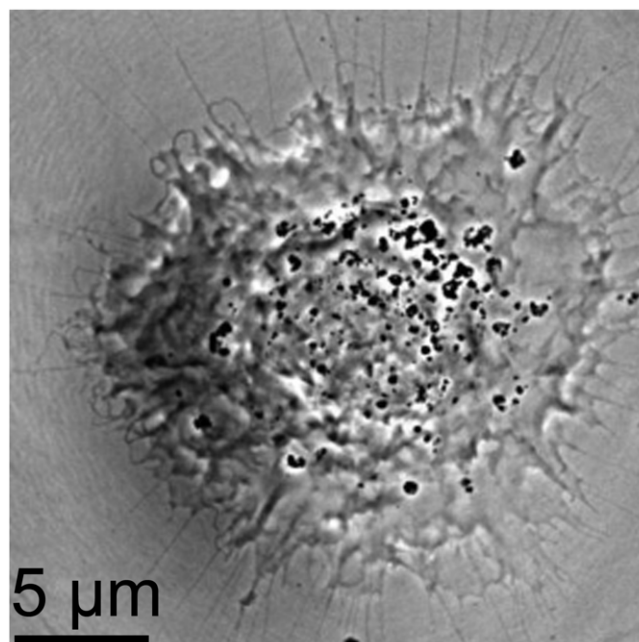


**Figure 12.** Micrograph of a HeLa cancer cell with bare Au nanoparticles and agglomerates (the dark spots) accumulated at the periphery of the nuclei.

defects. This result demonstrated the capability of the new radiology to solve long-standing issues in this domain.

Other relevant recent examples concern the electrodeposition of ramified Zn or Cu on Cu, and Ni on Cu [71–73]. In each case, the microradiology images and movies revealed fine details of the interplay between the local morphology and other parameters. Once again, the role of bubbles was found to be important and ubiquitous.

More recently, this line of research re-visited the electrodeposition of Cu on Au improving the space resolution with respect to previous studies. This revealed, for example, the details of the nucleation process.

Microradiology thus becomes a challenge to chronoamperometry, the standard method for studying nucleation in electrodeposition. Chronoamperometry is an important method in electrochemical research [74, 75], notably to explore metal nucleation by analysing the fluctuation in the transient current. This approach can, for example, clarify nucleation features such as the two-dimensional or three-dimensional character, or the instantaneous or progressive growth [76, 77]. Such features are important since they can determine the quality of the film.

Chronoamperometry, however, has some limitations and does not directly and locally detect the growth morphology. This is where microradiology can play an important role, revealing the initial stages of nucleation and specifically the evolution of individual islands.

We applied this approach to the electrodeposition of copper, whose industrial importance is well known, for example in microelectronics [78, 79]. We found that microradiology offers advantages not only with respect to chronoamperometry but also compared with other imaging techniques. Atomic force microscopy [80–84], for example,

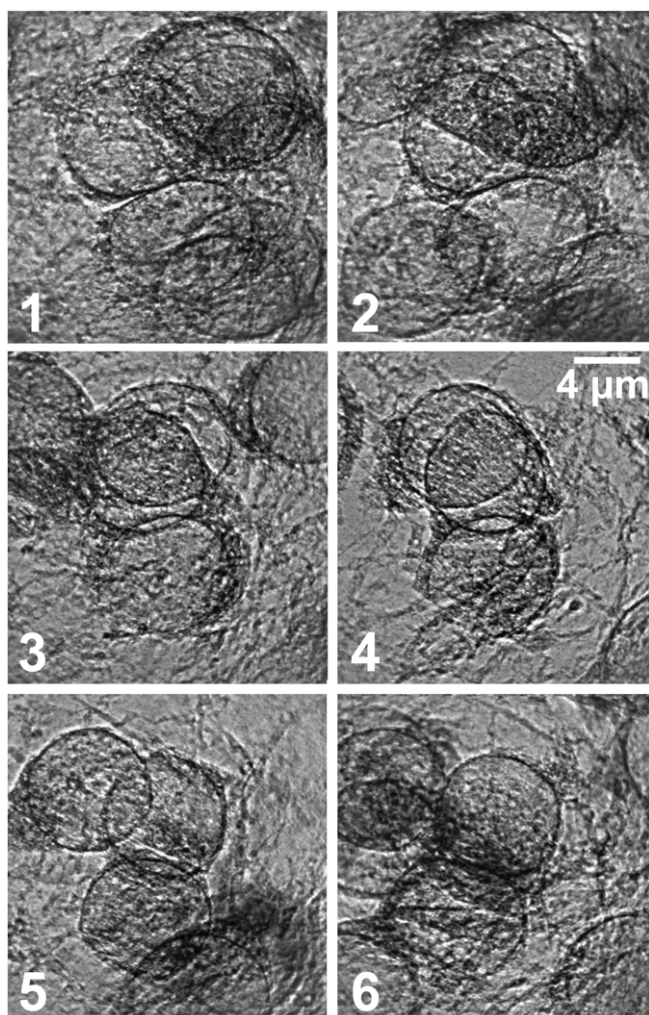


**Figure 13.** Six of the 280 raw projection images of neuron cells from mouse brain constituting a set used for tomographic reconstruction.

encounters difficulties in dealing with large height variations and has long image-taking times. Scanning electron microscopy can only take images after each growth step [85–87]. Transmission electron microscopy works only up to a certain thickness [88–90].

X-ray microscopy automatically eliminates all these problems. In the case of copper deposition, we could directly monitor the growth of individual clusters revealing their growth mechanisms. Depending on the electrolyte concentration, we detected either three-dimensional progressive growth or three-dimensional instantaneous growth.

#### 4.1. Experimental procedure

Electrodeposition was performed with the three-electrode approach. The counter and reference electrodes were 100  $\mu\text{m}$  Pt and 20  $\mu\text{m}$  Cu foils, cut to an L-shape and inserted in a specially designed miniature cell with the working electrode. The cell consisted of two Si wafers coated with a 1  $\mu\text{m}$   $\text{SiN}_3$  layer, separated by a 500  $\mu\text{m}$  thick Si wafer. Each lateral wafer was etched to create a 1.5  $\times$  1.5  $\text{mm}^2$  window transparent to x-rays.

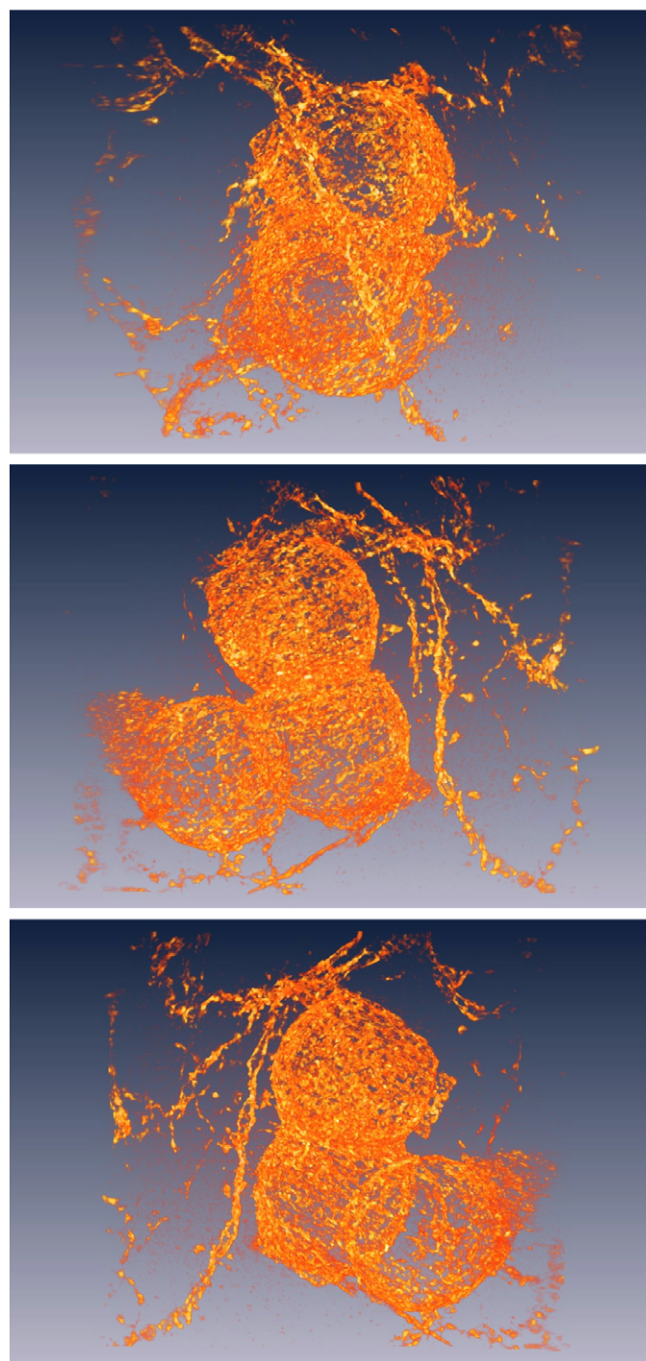


**Figure 14.** Three examples of tomography reconstructed images from the raw set of figure 13.

On one window, we built the working electrode by evaporating 50 nm of Au on a 10 nm Cr adhesion layer. Isolation between the working electrode and the other electrodes was guaranteed by coating the Au layer with a 35  $\mu\text{m}$  thick insulating SU-8 photoresist film. Within the film there was a 0.5  $\times$  0.5  $\text{mm}^2$  square window patterned by ultraviolet lithography, so that the SU-8 structure was a square ring.

The electrolyte was analytical grade  $\text{CuSO}_4$  (99.5%, SHOWA, Japan) mixed with 0.5M  $\text{H}_2\text{SO}_4$  (95%, Sigma, Switzerland) in deionized water. We used five different molar concentrations: 0.05M, 0.09M, 0.13M, 0.17M and 0.21M. All

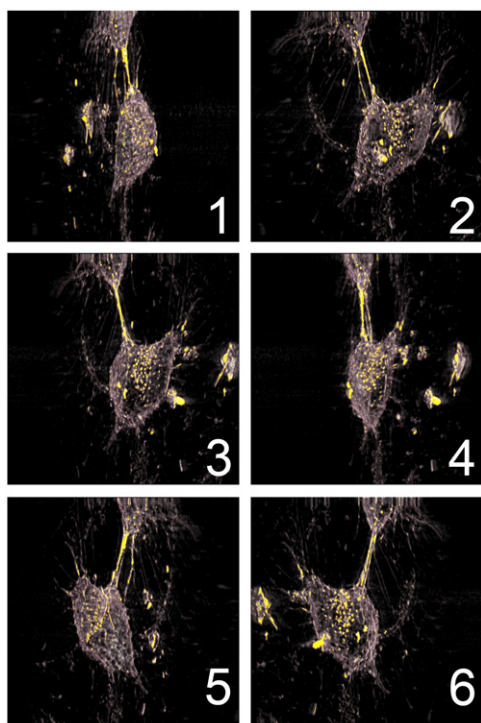


**Figure 15.** Six tomography reconstructed images of a HeLa cell with bare Au nanoparticles, similar to that of figure 12.

the electrodepositions were performed at room temperature by applying a  $-0.5$  V bias with an Autolab potentiostat-galvanostat (PGSTAT 30, Metrohm Autolab BV, Netherlands).

Transmission x-ray microscopy was performed at the 32-ID beamline of the Advanced Photon Source, Argonne National Laboratory, and at the 01B beamline of the Taiwan National Synchrotron Radiation Research Center. Our full field microscope uses a set of capillary condensers to shape the monochromatic x-ray beam and focus it on the object. The magnifying element was an Au FZP with 40 nm outermost zone width and 110 nm diameter.

#### 4.2. Results and discussion

The main objective of the experiments was to identify the dynamics of the nucleation mechanism based on the work of Scharifker and Hills [91]. One can distinguish between two mechanisms, instantaneous and progressive. Progressive nucleation corresponds to a slow growth of nuclei on a small and increasing number of active sites, activated during electroreduction. Instantaneous nucleation corresponds instead to the fast growth of nuclei on many active sites, all activated at the same time [92].

The theoretical models for instantaneous and progressive nucleation predict a peak in the current versus time curves obtained by chronoamperometry. By best fitting the theoretical forms to the curve, one could in principle distinguish between progressive and instantaneous growth [91]. In our case, however, this was not possible because chronoamperometry gave no peak at all—see figure 16.

We could speculate that bubble adsorption is the cause of peak absence. A bubble is indeed seen in the microradiograph

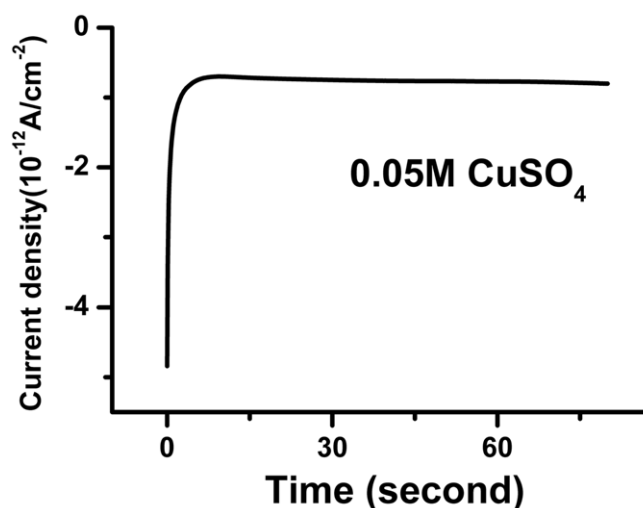


**Figure 16.** Transient current measured during the electrodeposition of Cu. The electrolyte composition was 0.05M  $\text{CuSO}_4$  and 0.5M  $\text{H}_2\text{SO}_4$ , and the applied voltage was  $-0.5$  V.

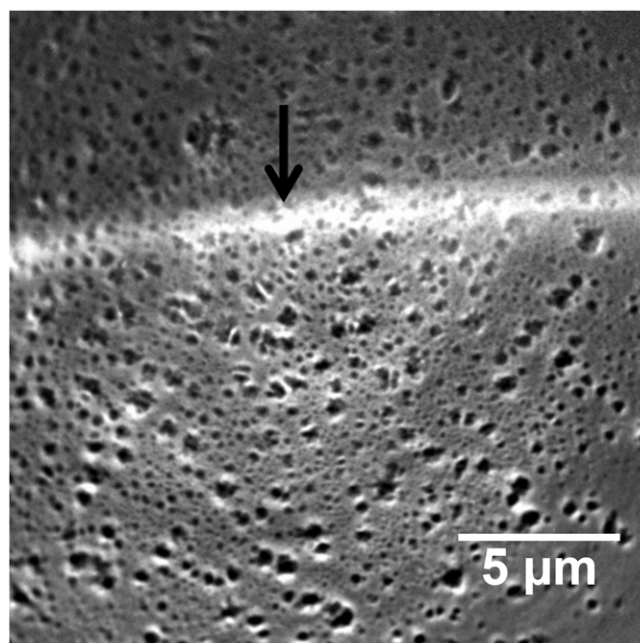


**Figure 17.** X-ray microradiograph taken during the electrodeposition. The arrow marks the boundary of a hydrogen bubble.

of figure 17, taken with Zernike phase contrast. Whatever the reason for the peak absence, the bottom line is that chronoamperometry cannot help us in identifying the growth mechanism.

By contrast, microradiology can dynamically detect the growth, as shown for example in figure 18, where we see Cu clusters produced by a 0.05M  $\text{CuSO}_4$  electrolyte. The microradiographs were taken 2, 10, 20, 30, 40 and 50 s after the beginning of electrodeposition. We see new clusters being gradually generated: this immediately identifies the growth mechanism as progressive.

We marked in figure 18 as ‘1’ and ‘2’ two groups of clusters whose growth initiated at different times, approximately 10 and

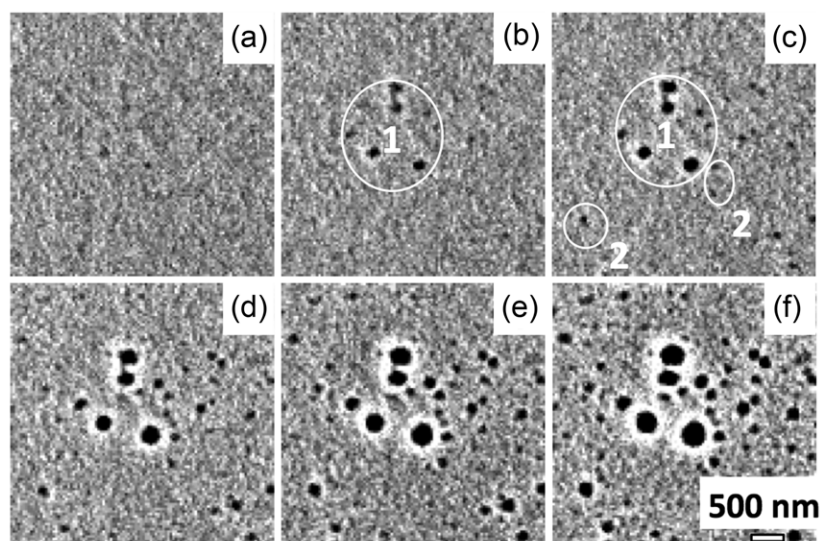


**Figure 18.** X-ray microradiographs taken during Cu electrodeposition with the same conditions as the previous two figures. The images were taken (a) 2, (b) 10, (c) 20, (d) 30, (e) 40 and (f) 50 s after the electrodeposition started. The white circles mark two groups of clusters whose growth initiated at two different times, providing direct evidence for the progressive growth mode.

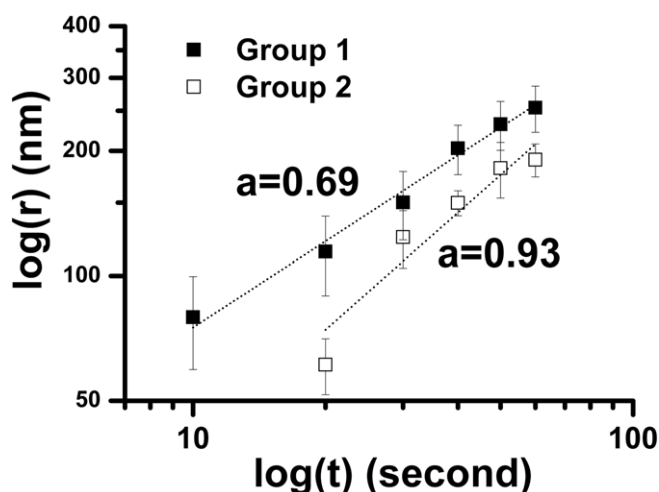


**Figure 19.** Log–log plot of the average cluster diameter as a function of time for the two groups marked in the previous figure.

20 s. Note, however, that the spatial resolution was limited in this case to 45 nm in order to take images in a short time: smaller clusters could not be reliably detected.

By analysing the cluster size growth with time, we revealed an interesting feature: the growth is different for clusters starting at different times. This can be seen from the log–log plots of figure 19 for the cluster groups ‘1’ and ‘2’: the curves suggest a  $r = At^a$  law, where  $r$  is the radius,  $t$  is the time and  $A$  is a constant. The value of  $a$  is markedly different for the two groups: 0.69 for group 1 and 0.93 for group 2.

Theoretically [90], for the clusters that begin immediately to grow we expect a diffusion-limited mechanism leading to hemispherical shapes. The cluster being reasonably far from each other, the diffusion for one of them does not affect the neighbours. This gives an  $r = At^{1/2}$  law.

Radisic *et al* [89, 90] found with transmission electron microscopy that this regime only lasts for 1–3 s. Afterwards, the diffusion areas for different clusters start to overlap and the

expected law is  $r = At^{1/6}$ . Qualitatively, these theoretical values are consistent with the decrease in the parameter  $a$  with time derived from figure 19. Quantitatively, however, our values are larger than the corresponding theoretical values  $1/2 = 0.5$  and  $1/6 = 0.17$ . This raises some questions about the diffusion model and its applicability.

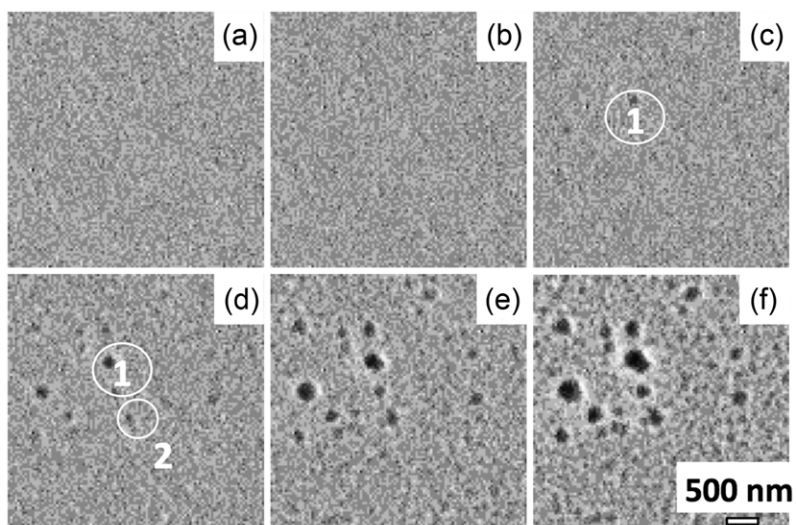
Can x-ray microscopy also detect instantaneous growth? We addressed this issue by forcing the growth to become instantaneous: this was accomplished by increasing the electrolyte concentration. Figures 20–23 show the cluster growth for different concentrations. We note the change in the growth regime: in figure 20, the number of nucleation sites progressively increases with time, as in figure 18. In figures 21–23, the nucleation sites are all activated at the same time.

Figure 24 summarizes the results for the two regimes by showing the number of clusters per unit area as a function of time. We clearly see the increase for the two cases of progressive growth, and the constant behaviour for the other three. In addition, note that the rate of increase is larger for the smaller electrolyte concentration. And the constant number of clusters per unit area is higher for the higher electrolyte concentrations in the second regime.

The two different growth modes also correspond to different growth laws. To probe this point, we analysed the growth for individual clusters and derived the exponent of the growth law as for figure 19. The results are shown in figure 25 as distribution histograms of the law exponents, for different electrolyte concentrations. For the progressive mode, we see mostly low values, below 1. For the instantaneous mode, larger values prevail.

## 5. Future trends

The techniques discussed in this paper did not reach their ultimate performances and significant improvements can be



**Figure 20.** X-ray microradiographs during Cu electrodeposition with a 0.09M CuSO<sub>4</sub> electrolyte, taken (a) 3, (b) 12, (c) 21, (d) 30, (e) 39 and (f) 48 s after the electrodeposition started. Here again we see progressive growth.

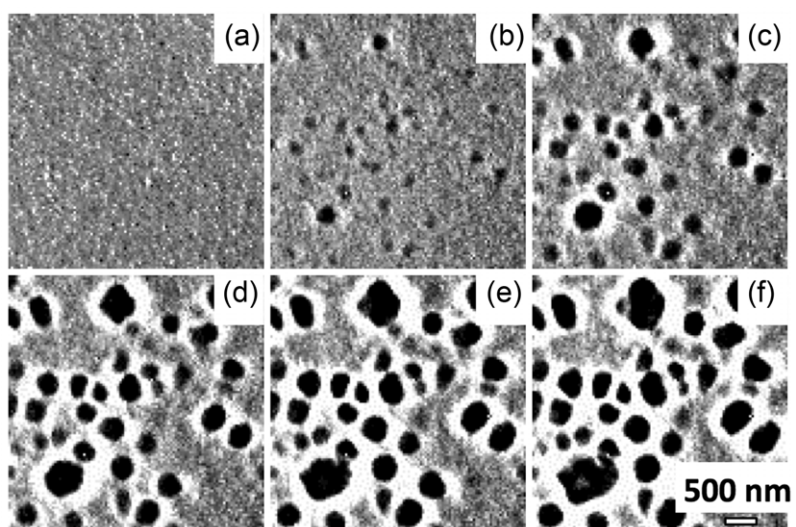


**Figure 21.** X-ray microradiographs for a 0.13M CuSO<sub>4</sub> electrolyte, taken at (a) 0, (b) 3, (c) 6, (d) 9, (e) 12 and (f) 15 s, indicating instantaneous growth.

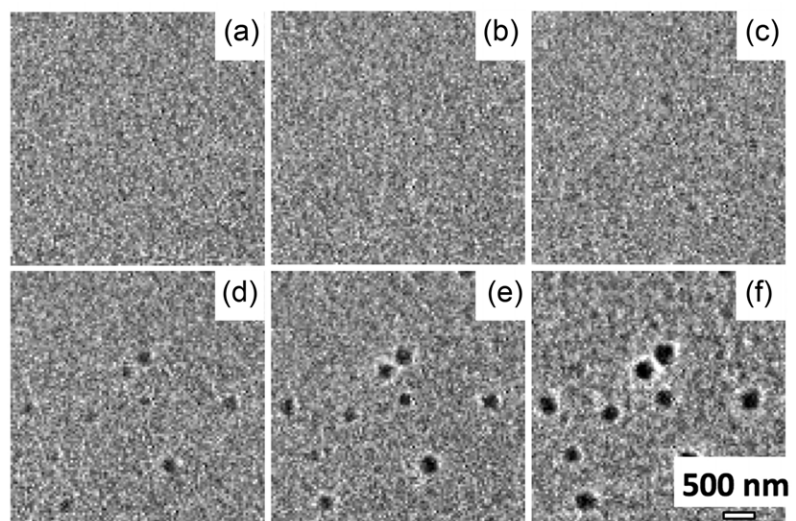


**Figure 22.** X-ray microradiographs for a 0.17M CuSO<sub>4</sub> electrolyte, taken at (a) 3, (b) 9, (c) 15, (d) 21, (e) 27 and (f) 33 s, again indicating instantaneous growth.

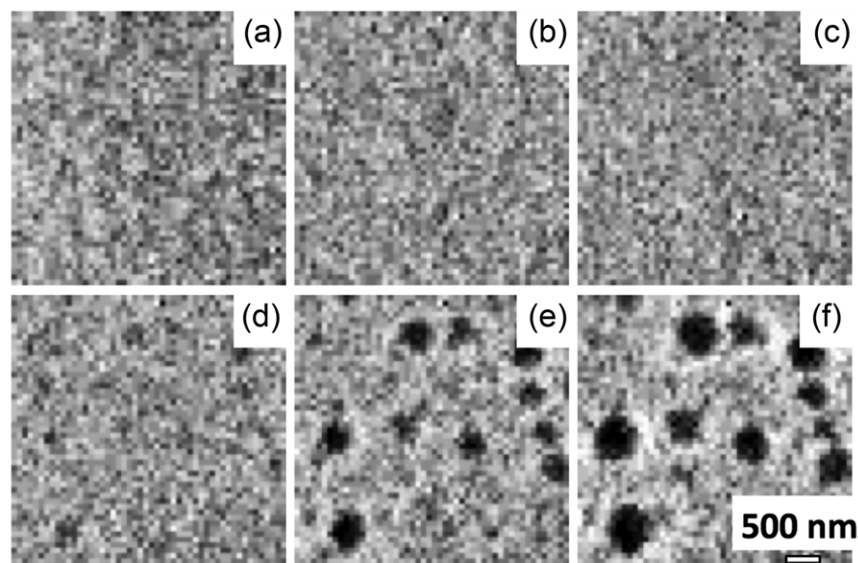


**Figure 23.** X-ray microradiographs for a 0.21M  $\text{CuSO}_4$  electrolyte, taken at (a) 0, (b) 3, (c) 6, (d) 9, (e) 12 and (f) 15 s, indicating instantaneous growth as the two previous figures.

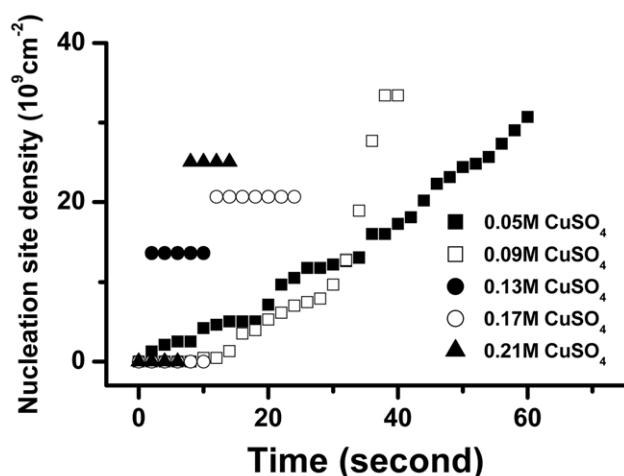


**Figure 24.** Nucleation site density as a function of time for different electrolytes.

expected in several directions. The staining procedures can become more effective, specifically as far as the fraction of stained cells is concerned. The FZP fabrication procedure can be further improved in several respects. As seen, the landmark of 10 nm resolution is at a reaching distance, and even that is unlikely to be the ultimate level.

In more general terms, all x-ray imaging techniques will certainly profit from the revolution underway in source technology. Quite recently, the first X-FEL was commissioned at Stanford [93]. And, as mentioned, the mechanism of seeding for X-FELs was successfully demonstrated at the FERMI X-FEL in Trieste (Elettra laboratory) [17]. X-FELs are bringing to imaging unprecedented levels of peak brightness, several orders of magnitude higher than synchrotrons. Furthermore, they bring full (diffraction limited) space coherence over their entire spectral range. And, with seeding, the time coherence also becomes extremely high. Imaging techniques based on phase contrast will certainly profit from the new levels of coherence.

However, FZPs have not been used so far in X-FELs. Additional work in fabrication, even about the basic structure, is required to enable FZPs to perform under the very intense emission. Several ideas were proposed, including using alternate materials such as diamond [38, 39] to construct the nanostructures to achieve long-term stability. One could also envision high throughput fabrication [94, 95] so that the zone plates become ‘disposable’ considering the relative low repetition rate of X-FELs. Some applications, such as using FZP to image the x-ray stimulated fluorescence, do not require the device to handle intense x-rays and are feasible without major modifications of the current FZP fabrication technology.

Microradiology, however, does not need to wait for these future improvements to strongly contribute to life science and materials science research. The examples presented in this review shows that the present performances are quite good for this task. The forthcoming progress will further broaden its impact and open entirely new domains of applications, in particular for fine radiology at the subcellular level.

## Acknowledgments

The authors thank all the colleagues from the Academia Sinica, the Mackay Memorial Hospital, the Tri-Service General Hospital, the Tsing Hua University, the National Synchrotron Radiation Research Center, the Argonne Advanced Photon Source, the Brookhaven National Synchrotron Light Source, the University of Bordeaux, the Ecole Polytechnique Fédérale de Lausanne (EPFL) and the Paul-Scherrer-Institut who participated in different stages of their imaging programmes. The research was supported by the National Science and Technology Programme for Nanoscience and Nanotechnology, the National Science Council, the Academia Sinica, the Fonds National Suisse pour la Recherche Scientifique, the EPFL, the Center for Biomedical Imaging (CIBM) and the

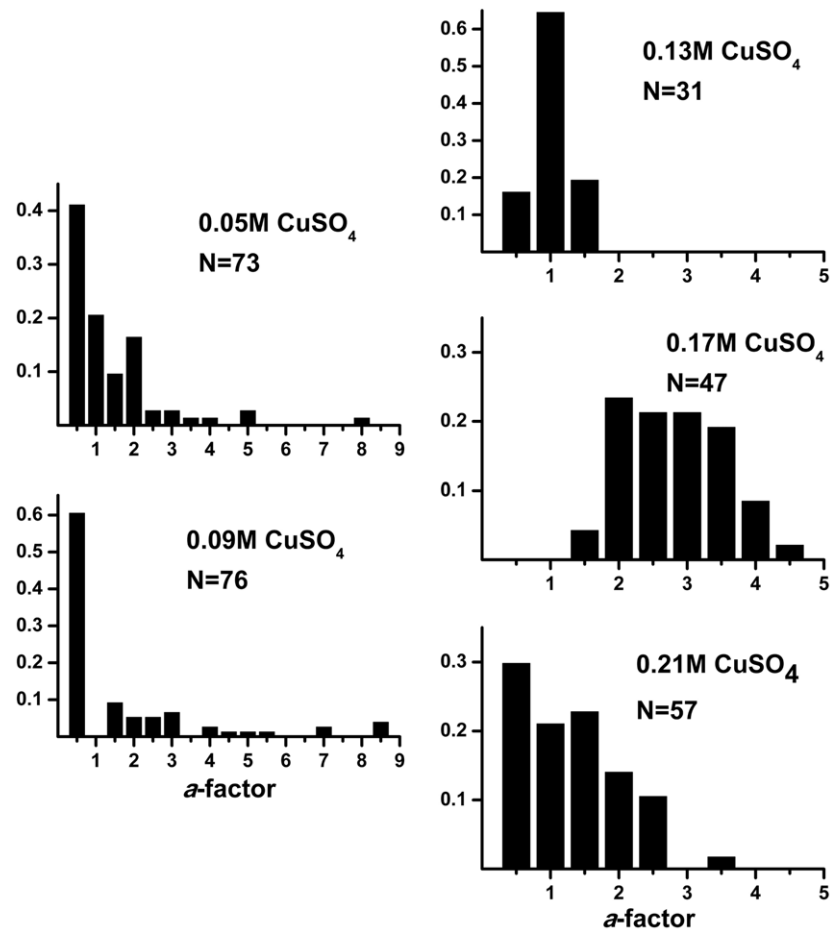


**Figure 25.** Normalized  $a$ -factor distributions measured for individual clusters; the different distributions correspond to different electrolytes.  $N$  is the number of clusters analysed for each electrolyte.

Brookhaven Science Associates, LLC under Contract No DE-AC02-98CH10886. Use of the Advanced Photon Source is supported by the US Department of Energy, Office of Basic Energy Sciences, under Contract No DE-AC02-06CH11357.

## References

- [1] Roentgen W 1896 *Nature* **53** 274
- [2] Howells M, Jacobsen C and Warwick T 2007 Principles and applications of zone plate x-ray microscopes *Science of Microscopy* vol II, ed P W Hawkes and J C H Spence (New York: Springer) pp 835–926
- [3] Fitzgerald R 2000 *Phys. Today* **53** 23
- [4] Wilkins S W, Gureyev T E, Gao D, Pogany A and Stevenson A W 1996 *Nature* **384** 335
- [5] Davis T J, Gao D, Gureyev T E, Stevenson A W and Wilkins S W 1995 *Nature* **373** 595
- [6] Momose A, Takeda T, Itai Y and Hirano K 1996 *Nature Med.* **2** 473
- [7] Margaritondo G, Hwu Y and Je J H 2005 *Riv. Nuovo Cimento* **27** 1
- [8] Spiller E A 1994 *Soft X-Ray Optics* (Bellingham, WA: SPIE) p 81
- [9] Attwood D 2007 *Soft X-Rays and Extreme Ultraviolet Radiation: Principles and Applications* (Cambridge: Cambridge University Press)
- [10] Cremer J T 2013 *Neutron and X-ray Optics* (Waltham, MA: Elsevier) chapter 10
- [11] Bass M, DeCusatis C, Enoch J, Lakshminarayanan V, Li G, MacDonald C, Mahajan V and Van Stryland E 2009 Zone plates *Handbook of Optics* 3rd edn, vol V *Atmospheric Optics, Modulators, Fiber Optics, X-Ray and Neutron Optics* (New York: McGraw-Hill) chapter 40
- [12] Margaritondo G 2002 *Elements of Synchrotron Light for Biology, Chemistry, and Medical Research* (New York: Oxford University Press)
- [13] Wu S-R, Hwu Y and Margaritondo G 2012 *Materials* **5** 1752
- [14] Wu H R 2012 *J. Phys. D: Appl. Phys.* **45** 242001
- [15] Tsai W L, Hsu P C, Hwu Y, Chen C H, Chang L W, Je J H, Lin H M, Groso A and Margaritondo G 2002 *Nature* **417** 139
- [16] Margaritondo G and Rebernik Ribic P 2011 *J. Synchrotron Radiat.* **18** 101
- [17] Allaria E *et al* 2012 *Nature Photon.* **6** 699
- [18] Lo T N *et al* 2007 *J. Phys. D: Appl. Phys.* **40** 3172
- [19] Chen Y T *et al* 2008 *J. Synchrotron Radiat.* **15** 170
- [20] Chu Y S *et al* 2008 *Appl. Phys. Lett.* **92** 103119
- [21] Chen Y T *et al* 2008 *Nanotechnology* **19** 395302
- [22] Chen Y T, Chen T Y, Yi J, Chu Y S, Lee W K, Wang C L, Kempson I M, Hwu Y, Gajdosik V and Margaritondo G 2011 *Opt. Lett.* **36** 1269
- [23] Chen T Y, Chen Y T, Wang C L, Kempson I M, Lee W K, Chu Y S, Hwu Y and Margaritondo G 2011 *Opt. Express* **21** 19919
- [24] Holmberg A *et al* 2011 *AIP Conf. Proc.* **1365** 18
- [25] Reinspach J, M Lindblom, Hofsten O, Bertilson M, Hertz H M and Holmberg A 2010 *Microelectron. Eng.* **87** 1583

- [26] Chubarova E, Nilsson D, Lindblom M, Reinspach J, Birch J, Vogt U, Hertz H M and Holmberg A 2011 *Microelectron. Eng.* **88** 3123
- [27] Mayer M, Grévent C, Szeghalmi A, Knez M, Weigand M, Rehbein S, Schneider G, Baretzky B and Schütz G 2011 *Ultramicroscopy* **111** 1706
- [28] Koyama T, Takano H, Konishi S, Tsuji T, Takenaka H, Ichimaru S, Ohchi T and Kagoshima Y 2012 *Rev. Sci. Instrum.* **83** 013795
- [29] Chien C C, Chen H H, Lai S F, Wu K C, Cai X, Hwu Y, Petibois C, Chu Y and Margaritondo G 2012 *J. Nanobiotechnology* **10** 10
- [30] Yin G C, Song Y F, Tang M T, Chen F R, Liang K S, Duewer F W, Feser M, Yun W B and Shieh H P D 2006 *Appl. Phys. Lett.* **89** 221122
- [31] Gorelick S, Vila-Comamala J, Guzenko V A, Barrett R, Salome M and David C 2011 *J. Synchrotron Radiat.* **18** 442
- [32] Feng Y, Feser M, Lyon A, Rishon S, Zeng X, Chen S, Sassolini S and Yun W 2007 *J. Vac. Sci. Technol. B* **25** 2004
- [33] Werner S, Rehbein S, Guttmann P, Heim S and Schneider G 2010 *Microelectron. Eng.* **87** 1557–60
- [34] Kagoshima Y, Takano H, Koyama T, Tsusaka Y and Saikubo A 2011 *Japan J. Appl. Phys.* **50** 022503
- [35] Berujon S, Wang H, Pape I, Sawhney K, Rutishauser S and David C 2012 *Opt. Lett.* **37** 1622
- [36] Nilsson D, Uhlén F, Reinspach J, Hertz H M, Holmberg A, Sinn H and Vogt U 2012 *New J. Phys.* **14** 043010
- [37] Kuwabara H, Yashiro W, Harasse S, Mizutani H and Momose A 2011 *Appl. Phys. Express* **4** 062502
- [38] Uhlén F, Lindqvist S, Nilsson D, Reinspach J, Vogt U, Hertz H M and Holmberg A 2011 *J. Vac. Sci. Technol. B* **29** 06FG03
- [39] David C *et al* 2011 *Sci. Rep.* **1** 57
- [40] Wojcik M, Joshi J V, Sumant A V, Divan R, Ocola L E, Lu M and Mancini D C 2010 *J. Vac. Sci. Technol. B* **28** C6P30
- [41] Sarkar S S, Solak H H, Raabe J, David C and van der Veen J F 2010 *Microelectron. Eng.* **87** 854
- [42] Gorniak T *et al* 2011 *Opt. Express* **19** 11059
- [43] Chao W, Fischer P, Tylliszczak T, Rekawa S, Anderson E and Naulleau P 2012 *Opt. Express* **20** 9777
- [44] Rehbein S, Guttmann P, Werner S and Schneider G 2012 *Opt. Express* **20** 5830
- [45] Liese T, Radisch V, Knorr I, Reese M, Großmann P, Mann K and Krebs H-U 2011 *Appl. Surf. Sci.* **257** 5138
- [46] Yi J, Chu Y S, Chen Y T, Chen T Y, Hwu Y and Margaritondo G 2011 *J. Phys. D: Appl. Phys.* **44** 232001
- [47] Kirz J 1974 *J. Opt. Soc. Am.* **64** 301
- [48] Mayer M, Keskinbora K, Grévent C, Szeghalmi A, Knez M, Weigand M, Snigirev A, Snigireva I and Schütz G 2013 *J. Synchrotron Radiat.* **20** 433
- [49] Chien C C *et al* 2013 *Biotechnol. Adv.* **31** 375
- [50] Withers P J 2007 *Mater. Today* **10** 26
- [51] Neuhäusler U, Schneider G, Ludwig W, Meyer M A, Zschech E and Hambach D 2003 *J. Phys. D: Appl. Phys.* **36** A79
- [52] Holzner C, Feser M, Vogt S, Hornberger B, Baines S B and Jacobsen C 2010 *Nature Phys.* **6** 883
- [53] Rehbein S, Heim S, Guttmann P, Werner S and Schneider G 2009 *Phys. Rev. Lett.* **103** 110801
- [54] Suzuki Y, Takeuchi A, Takenaka H and Okada I 2010 *X-ray Opt. Instrum.* **2010** 824837
- [55] Sunaguchi N, Yuasa T, Huo Q, Ichihara S and Ando M 2010 *Appl. Phys. Lett.* **97** 153701
- [56] Miao J, Charalambous P, Kirz J and Sayre D 1999 *Nature* **400** 342
- [57] Nugent K A, Peele A G, Chapman H N and Mancuso A P 2003 *Phys. Rev. Lett.* **91** 203902
- [58] Miao J, Hodgson K O, Ishikawa T, Larabell C A, LeGros M A and Nishino Y 2003 *Proc. Natl Acad. Sci. USA* **100** 110
- [59] Giewekemeyer K, Thibault P, Kalbfleisch S, Beerlink A, Kewish C M, Dierolf M, Pfeiffer F and Salditt T 2010 *Proc. Natl Acad. Sci. USA* **107** 529
- [60] Shapiro D *et al* 2005 *Proc. Natl Acad. Sci. USA* **102** 15343
- [61] Chao W, Harteneck B D, Liddle J A, Anderson E H and Attwood D T 2005 *Nature* **435** 1210
- [62] Jacobsen C 1999 *Trends Cell Biol.* **9** 44
- [63] Meyer-Ilse W, Hamamoto D, Nair A, Lelievre S A, Denbeaux G, Johnson L, Pearson A L, Yager D, Legros M A and Larabell C A 2001 *J. Microsc.* **201** 395
- [64] Larabell C A and Le Gros M A 2004 *Mol. Biol. Cell* **15** 957
- [65] Le Gros M A, McDermott G and Larabell C A 2005 *Curr. Opin. Struct. Biol.* **15** 593
- [66] Parkinson D Y, McDermott G, Etkin L D, Le Gros M A and Larabell C A 2008 *J. Struct. Biol.* **162** 380
- [67] McDermott G, Le Gros M A, Knoechel C G, Uchida M and Larabell C A 2009 *Trends Cell Biol.* **19** 587
- [68] Nakajima K 2008 *Nature Phys.* **4** 92
- [69] Corde S, Ta Phuoc K, Beck A, Lambert G, Fitour R, Lefebvre E, Malka V and Rousse A, arXiv:1301.5066v1 [physics.plasm-ph]
- [70] Lundh O *et al* 2011 *Nature Phys.* **7** 219
- [71] Hsu P C *et al* 2008 *J. Electrochem. Soc.* **155** D400
- [72] Hsu P, Chu Y S, Yi J, Wang C L, Wu S R, Hwu Y and Margaritondo G 2010 *Appl. Phys. Lett.* **97** 033101
- [73] Hsu P C, Lin C S, Hwu Y, Je J H and Margaritondo G 2010 *Electrocatalysis: Computational, Experimental and Industrial Aspects* ed C F Zinola (Boca Raton, FL: CRC Press) p 479
- [74] Bonou L, Eyraud M, Denoyel R and Massiani Y 2002 *Electrochim. Acta* **47** 4139
- [75] Bard A J and Faulkner L R 2001 *Electrochemical Methods Fundamentals and Applications* 2nd edn (New York: Wiley)
- [76] Hwang B J, Santhanam R, Wu C R and Tsai Y W 2001 *J. Solid State Electrochem.* **5** 280
- [77] Hwang B J, Santhanam R and Lin Y L 2001 *Electrochim. Acta* **46** 2843
- [78] Andricacos P C, Uzoh C, Dukovic J O, Horkans J and Deligianni H 1998 *IBM J. Res. Dev.* **42** 567
- [79] Schlesinger M and Paunovic M 2000 *Modern Electroplating* 4th edn (New York: Wiley)
- [80] Radisic A, West A C and Searson P C 2002 *J. Electrochem. Soc.* **149** C94
- [81] Smith E L, Barron J C, Abbott A P and Ryder K S 2009 *Anal. Chem.* **81** 8466
- [82] Kang M and Gewirth A A 2003 *J. Electrochem. Soc.* **150** C426
- [83] Grujicic D and Pesic B 2002 *Electrochim. Acta* **47** 2901
- [84] Sahari A, Azizi A, Schmerber G and Dinia A 2008 *Surf. Rev. Lett.* **15** 717
- [85] Liu H, Favier F, Ng K, Zach M P and Penner R M 2001 *Electrochim. Acta* **47** 671
- [86] Shao W, Pattanaik G and Zangari G 2007 *J. Electrochem. Soc.* **154** D339
- [87] Bicer M and Sisman I 2011 *Appl. Surf. Sci.* **257** 2944
- [88] Radisic A, Vereecken P M, Searson P C and Ross F M 2006 *Surf. Sci.* **600** 1817
- [89] Radisic A, Vereecken P M, Hannon J B, Searson P C and Ross F M 2006 *Nano Lett.* **6** 238
- [90] Radisic A, Ross F M and Searson P C 2006 *J. Phys. Chem. B* **110** 7862
- [91] Scharifker B and Hills G 1983 *Electrochim. Acta* **28** 879
- [92] Pardave M P, Ramirez M T, Gonzales I, Serruya A and Scharifker B R 1996 *J. Electrochem. Soc.* **143** 1551
- [93] Emma P *et al* 2010 *Nature Photon.* **4** 641
- [94] Keskinbora K *et al* 2013 *Opt. Express* **21** 11747
- [95] Altissimo M, Romanato F, Vaccari L, Businaro L, Cojoc D, Kaulich B, Cabrini S and Di Fabrizio E 2002 *Microelectron. Eng.* **61** 173